An Adsorptive Membrane Platform for Precision Ion Separation: Membrane Design and First-Principles Studies

Van T. C. Le, Quy P. Nguyen, Hien Duy Mai, Bin Wang, and Ngoc T. Bui*

One of the key challenges in separation science is the lack of precise ion separation methods and mechanistic understanding crucial for efficiently recovering critical materials from complex aqueous matrices. Herein, first-principles electronic structure calculations and in situ Raman spectroscopy are studied to elucidate the factors governing ion discrimination in an adsorptive membrane specifically designed for transition metal ion separation. Density functional theory calculations and in situ Raman data jointly reveal the thermodynamically favorable binding preferences and detailed adsorption mechanisms for competing ions. How membrane binding preferences correlate with the electronic properties of ligands is explored, such as orbital hybridization and electron localization. The findings underscore the importance of the phenolate group in oxime ligands for achieving high selectivity among competing transition metal ions. In-depth understanding on which specific atomistic site within the microenvironment of metal-ligand binding pockets governs the ion discrimination behaviors of the host will build a solid foundation to guide the rational design of next-generation materials for precision separation essential for energy technologies and environment remediation. In tandem, synthetic controllability is demonstrated to transform 3D micrometer-scale crystals to a 2D crystalline selective layer in membranes, paving the way for more precise and sustainable advances in separation science.

1. Introduction

Natural disasters, health crises, geopolitical instability, and technical disruptions are some of the factors intensifying the vulnerabilities of metal supply chains for modern technologies. These factors necessitate energy-efficient and highly selective methods

V. T. C. Le, Q. P. Nguyen, H. D. Mai, B. Wang, N. T. Bui School of Sustainable Chemical, Biological, and Materials Engineering The University of Oklahoma Norman, OK 73019, USA

E-mail: ngoctbui21@ou.edu

N. 1. Bul School of Civil Engineering and Environmental Science The University of Oklahoma Norman, OK 73019, USA

The ORCID identification number(s) for the author(s) of this article can be found under https://doi.org/10.1002/sstr.202400067.

© 2024 The Authors. Small Structures published by Wiley-VCH GmbH. This is an open access article under the terms of the Creative Commons Attribution License, which permits use, distribution and reproduction in any medium, provided the original work is properly cited.

DOI: 10.1002/sstr.202400067

to recover critical minerals from diverse water matrices, while concomitantly revitalizing these water streams and alleviating corresponding environmental issues at low waste management cost.[1,2] Besides essential elements characterized as having geopolitically concentrated production and low rates of end-of-life recycling, minerals skeletal of energy technologies, such as transition metal ions, are vital (2022 United States Geological Survey). [3a] Recently, in its critical materials assessment, the U.S. Department of Energy listed nickel, cobalt, and copper as critical and near critical in the medium-term (2025-2035) criticality matrix, respectively. [3b] Meanwhile, the existence of these trace elements in industrial discharges affects vast areas of freshwater reservoirs, [4] posing significant threats to the environment and public health if not treated effectively.

Efficient metal recovery requires materials and methods capable of precisely targeting desired ions from multi-ionic aqueous mixtures. Advancing science in precision ion separation is, thus, essential to innovate efficient and mature methods for a circular

economy of water, energy, and resources. Selective separation among metal ions with inherently similar properties is challenging, however. [5-7] Despite intensive efforts, current state-of-theart methods are often energy inefficient while generating large volumes of chemical waste. [7] Also, not many materials have been truly challenged to demonstrate separation among similar ions in multicomponent mixtures. [7g,8] Across various material platforms (e.g., adsorbent, membrane, electrode), one of the effective strategies involves utilizing surface functional groups to regulate ionic mobility and binding affinity between ions and material surfaces. [2,6-10] For instance, DuChanois and co-workers used polyelectrolyte multilayer membranes with iminodiacetate (IDA) functional groups to govern membrane selectivity toward similar transition metal ions in bi-cationic solutions^[6] and demonstrated a Cu²⁺/Ni²⁺ separating factor of <30. Other efforts involve the use of nanoporous and 2D materials, [8,11] such as graphene oxide and MoS2 nanosheets for metal ion removal based on adsorption via electrostatic, cation– π interactions, and others (Table S1, Supporting Information). For instance, Liu and coworkers studied the interactions of divalent ions with graphene oxide (GO) membranes and their roles in controlling mass transport through the membranes. The study showed that Cu²⁺ dominated the transport across the GO membranes with the

www.advancedsciencenews.com

equimolar coexistence of Ca²⁺ and Mg²⁺.^[11a] While these materials exhibit intriguing selective ion transport across membranes, mechanisms governing such selective behaviors have yet been thoroughly understood.

We recently discovered an emerging material based on a supramolecular framework, which we named ZIOS, constructed from zinc, 2-methylimidazole (MeIM), and salicylaldoxime (Sal) with outstanding copper adsorption kinetics, up to 50 times faster than that of the state-of-the-art copper adsorbent.^[12] Furthermore, ZIOS demonstrated excellent copper selectivity from a complex mixture having several coexisting ions. We hypothesized that the transmetalation between the guest metal ions and the zinc node in the host framework as well as the coordination between the guest metal ions and the active binding sites in the surrounding ligands play critical roles in governing adsorption behaviors of ZIOS. Still, the precise mechanism by which each of these mechanisms governs the ion discrimination capability of ZIOS remains unclear. Herein, we synergize firstprinciples electronic structure calculations and in situ Raman spectroscopy to elucidate the factors governing ion discriminating behaviors of ZIOS membranes toward the four transition metal ions that are inherently similar (i.e., Cu²⁺, Co²⁺, Ni²⁺, Mn²⁺). Such knowledge is inevitable to uncover guidelines for rationally designing advanced materials essential to transform separation to a more precise regime.

Furthermore, translation of ZIOS into macroscopic membrane platforms to enable continuous and efficient metal recovery processes is important. Membrane technologies, in general, provide energy-efficient, chemical-efficient, and economical solutions for advanced separation. [13] However, established polymeric membranes are often effective for broad-spectrum separation and therefore, unable to target specific species of interest from multicomponent mixtures. Herein, we present an effective adsorptive membrane platform where ZIOS crystals are controllably translated into a 2D membrane structure for precision ion separation. We fundamentally studied the membrane behaviors in selectively separating four competing transition metal ions and elucidated the underneath governing mechanisms with density functional theory (DFT)-based electronic structure calculations and in operando Raman analyses.

2. Results and Discussion

The translation of three-dimensional (3D) micrometer-scale rod-like ZIOS crystals^[12] into a two-dimensional (2D) selective layer of a composite membrane platform is inherently challenging. Recent advances in zeolite membranes^[14] have inspired us to develop controllable synthetic approaches in which the physicochemical properties of the reaction media are tuned to translate ZIOS crystals to adsorptive membranes effective for metal—ion separation. In essence, we appraise three different membrane synthesis methods, including stirring-assisted hydrothermal growth (method A), vacuum-assisted coordination growth (method B), and interfacial coordination growth (method C) for the design of ZIOS adsorptive membranes (schematically illustrated in **Figure 1**a). Of note, the PVDF substrate was first functionalized with PDA and PEI to facilitate the nucleation and growth of ZIOS layer in the next steps. Details of the synthetic

conditions for the surface modification and ZIOS deposition steps are described in the supporting information. In all three methods, we manipulate the elasticity of the reaction media by using poly (vinyl alcohol) (PVA) as a viscosity enhancer, thereby controlling ZIOS crystal morphology as they grow on the surface of the PVDF-PDA-PEI support layer (Figure 1a).

Among the inspected methods, stirring-assisted hydrothermal synthesis (method A) is a promising approach as it brings about the formation of a uniform layer of crystalline ZIOS on the membrane support (Figure S1a, Supporting Information). With the well-mixedness by coupling a stirring force during the hydrothermal process, crystal uniformity and morphology can be enhanced. Meanwhile, a less uniform ZIOS layer was observed for methods B and C (Figures S1B,C-S3, Supporting Information). Therefore, hereafter, we discuss the ion-separating behaviors observed in ZIOS membranes synthesized with method A. Results show that we successfully deposited ZIOS selective layers with uniform and well-packed crystals having hexagonal sheetlike morphology on the PVDF-PDA-PEI supports (Figure 1b,c). Also, the width of ZIOS grain increased from 0.69 to 3.26 µm while the sheet length decreased from 12.03 to 9.17 µm as PVA concentration increased from 0 to 0.5 and 1 wt%, respectively (Figure S4, Supporting Information). The thickness of the ZIOS selective layer, ranging from 5.4 to 18.0 µm, was controllably achieved via a two-step coating method (Figures 1d and S5, S6, Supporting Information).

2.1. Ion Separation Performance of ZIOS/PVDF-PDA-PEI Membranes

Because the most uniform membrane was obtained with 1 wt% of PVA, we selected this condition to study adsorption behaviors of membranes having 18 µm-thick ZIOS selective layers. For this specific membrane selective layer, each ZIOS grain has a dimension of $9.17 \,\mu\text{m} \times 3.26 \,\mu\text{m} \times 0.25 \,\mu\text{m}$ (length \times width \times thickness). To interrogate the preferential binding mechanisms, and hence selective adsorption behaviors, of ZIOS membranes toward similar transition metal ions in a multi-ionic environment, we challenged the membranes with an equimolar mixture of four competing transition cations having similar charge and solvated ionic radii (Figure 2b). We measured the adsorptive separating behaviors of ZIOS/PVDF-PDA-PEI membranes in a diffusion cell setup (Figure 2a) where the membranes were sandwiched between two compartments: 1) the feed with equimolar aqueous solutions of Co²⁺, Mn²⁺, Ni²⁺, and Cu²⁺ at different pH values (e.g., pH 2.5 and pH 5.0); and 2) the receiving compartment with deionized water. Results show that ZIOS membranes preferentially adsorbed Cu²⁺ at a high adsorption efficiency while negligibly capturing Co²⁺ and Mn²⁺ (Figures 2c and S7a,b) from these pH-varied ion mixtures. At pH 2.5, the separating performance of ZIOS membrane exceeds that of state-of-the-art Cu²⁺ separating membranes (Figure 2e, Table S1, Supporting Information), $^{[6,11a,15]}$ with calculated Cu^{2+}/Ni^{2+} , Cu^{2+}/Mn^{2+} , and Cu^{2+}/Co^{2+} separation factors of approximately 193, 2049, and 638, respectively (Figure 2d and S8, Supporting Information). Membrane performance under alkaline conditions are discussed in Figure S9 and S10, Supporting Information.



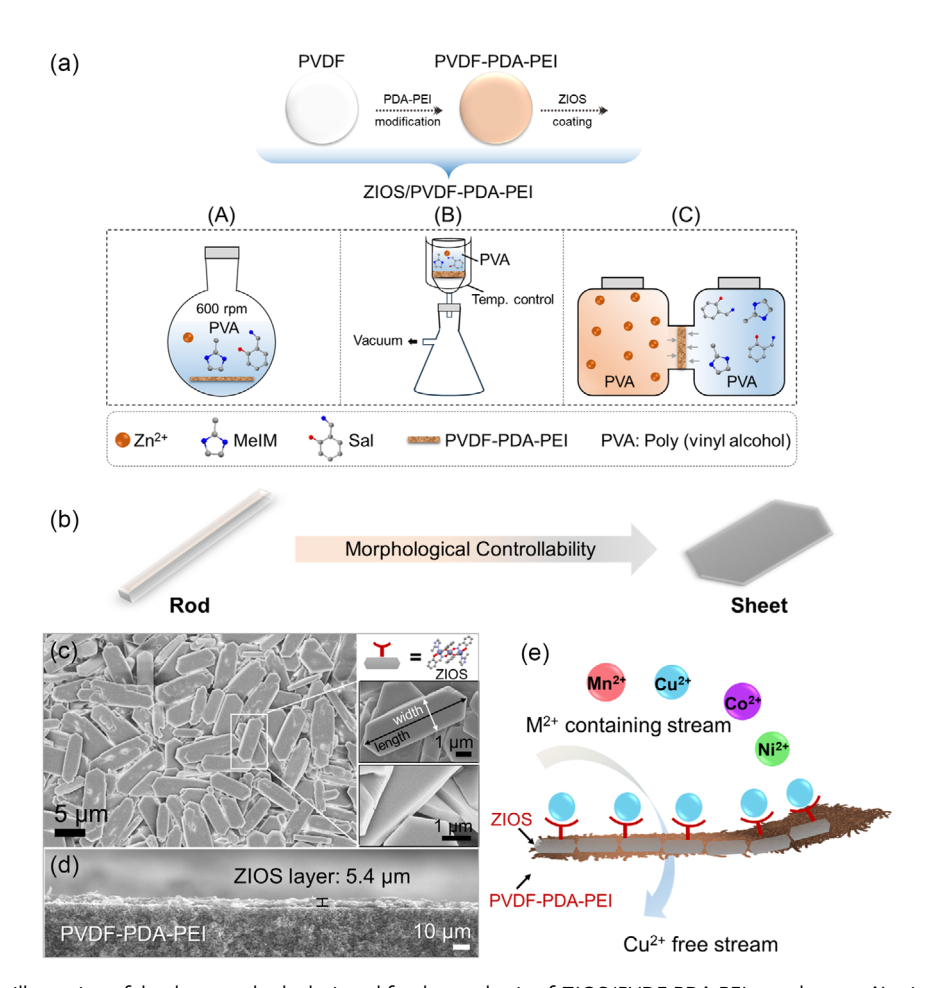


Figure 1. a) Schematic illustration of the three methods designed for the synthesis of ZIOS/PVDF-PDA-PEI membranes: A) stirring-assisted hydrothermal growth method, B) vacuum-assisted coordination growth method, and C) interfacial coordination growth method. b) Morphological controllability of ZIOS crystalline layer on the surface of the PVDF-PDA-PEI support in membrane synthesis. c) Representative top-view scanning electron microscopy (SEM) images of a ZIOS/PVDF-PDA-PEI membrane surface and individual ZIOS particles. d) Representative cross-sectional SEM image of ZIOS/PVDF-PDA-PEI membrane. e) Schematic illustration of ZIOS/PVDF-PDA-PEI membrane for selective ion separation from a mixture of four transition metal ions.

In addition, we observe a correlation between the total concentration of adsorbed cations (i.e., Cu²⁺, Ni²⁺, Co²⁺, and Mn²⁺) versus that of the released Zn2+ from ZIOS membranes (Figure S7c, Supporting Information). We defined n as the ratio of the former to the latter values and hypothesized that its change as a function of time is correlated to the pH-dependent adsorption mechanisms of ZIOS membranes. Specifically, there is an interplay of 1) the transmetalation between any of the four guest cations (M) and the host metal node Zn(II) ions, which results in the metal-exchanged ZIOS structures, denoted hereafter as M(II)-transmetalated ZIOS; and 2) the coordination of the guest cations to the active sites within the binding pockets in governing preferential metal binding behaviors of the membranes. An $n \le 1$, such as that observed in the case of pH 2.5 (Figure 2f) and S7d, Supporting Information), may suggest that transmetalation dominates the selective adsorption behaviors, whereas an $n \gg 1$ likely represents the case where the two mechanisms coexist. For instance, at pH 5, n steadily reduces from 1.67 (at 30 min) to 1.07 (at 180 min), highlighting the dominant role of coordination in metal-ion adsorption. We postulate that under this

condition, chemical cleavage occurs at the N_{MelM} and/or $O_{Hydroxyimino}$, leading to the creation of additional coordinative binding sites for metal adsorption. Once these ligand coordination sites are saturated, transmetalation takes over.

The differences in the mechanisms governing metal-ion capture also contribute to the variation in ion adsorption rates observed at two pH conditions. Specifically, the adsorption rate of Cu²⁺ at pH 2.5 is higher than that at pH 5.0, whereas the adsorption rates of Ni²⁺, Co²⁺, and Mn²⁺ are notably lower at pH 2.5 compared to pH 5.0. (Figure 2c). This discrepancy arises because the adsorption of Cu²⁺ relies on both transmetalation and side-chain coordination, whereas that of other guest ions (i.e., Ni²⁺, Co²⁺, Mn²⁺) is primarily governed by the latter mechanism. This results in distinct behaviors in the adsorption rates of each metal under different pH conditions. In the case of Ni²⁺, Co²⁺, and Mn²⁺adsorption, elevated pH conditions facilitate the deprotonation of the coordinative oxygen within the hydroxyamino group. This deprotonation process is responsible for the side-chain coordination, leading to a higher initial rate of ion capture for these metals. This phenomenon is further supported by www.advancedsciencenews.com

small structures

www.small-structures.com

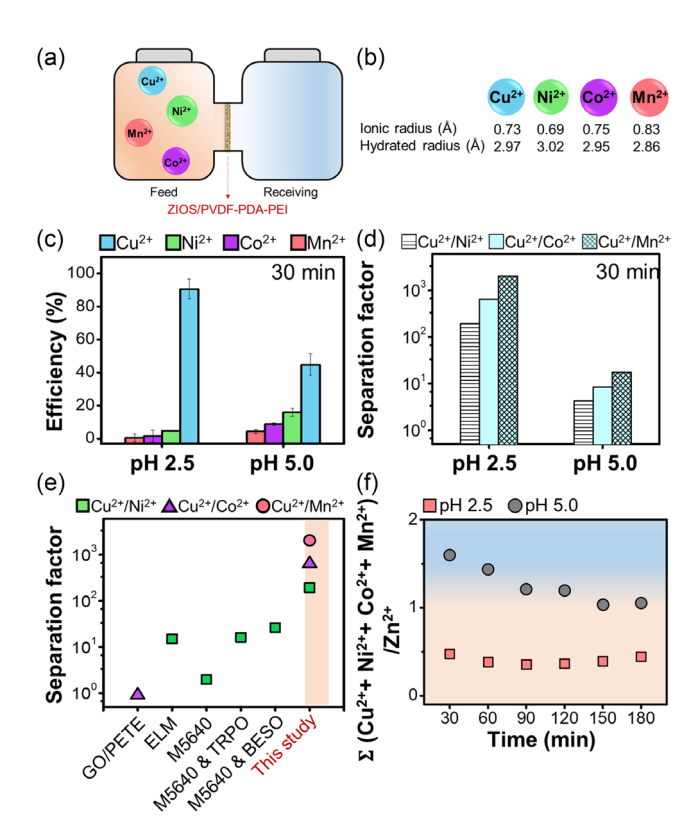


Figure 2. a) A diagram of our experimental setup for testing metal—ion capture behaviors of ZIOS membranes and b) ionic and hydrated radii of metal ions. [19] Adsorption behaviors of ZIOS/PVDF-PDA-PEI membranes in equimolar aqueous solutions of Cu^{2+} , Ni^{2+} , Co^{2+} , and Mn^{2+} (\approx 10 ppm each) at pH 2.5 and 5.0, c) adsorption efficiency, d) separation factor calculated at 30 min, e) a comparison of ion-selective capability of ZIOS/PVDF-PDA-PEI membrane versus other state-of-the-art ion selective membranes, and f) correlation between the total concentration of guest cations (Cu^{2+} , Ni^{2+} , Co^{2+} , and Mn^{2+}) versus that of released Zn^{2+} over time. Membranes with an active area diameter of 15 mm were utilized. Error bars denote \pm 1 standard deviation around the mean from three separate measurements.

Figure S7a,b and S9a, Supporting Information, illustrating the transition of adsorption efficiency for Ni²⁺, Co²⁺, and Mn²⁺ from the logarithm to the exponential trends, driven by the increased availability of side-chain chelates at the outset of the process. Conversely, we theorize that the rise in pH conditions from 2.5 to 5.0 shifts the equilibrium of Cu²⁺ species toward complexes with greater Cu hydroxide chelation, which could diminish the rate of Cu transmetalation. In addition, at pH 5.0, the side-chain coordination of Cu²⁺ appears to be less kinetically competitive with Ni²⁺ (**Figure 3**, S18, Supporting Information). As a result, the initial rate of Cu²⁺ adsorption (during the first 30 min) at pH 5.0 is lower than that at pH 2.5.

In sum, transmetalation appears to govern ZIOS adsorption behaviors in environments with high proton concentration, leading to an equivalence of the guest ion uptake versus host ion release. However, the dominant role of coordination in ZIOS binding behaviors leads to a higher guest ion uptake and a low Zn^{2+} release. Interestingly, the bond valence sum analysis using the observed bond distances in the crystal structure data

(Table S2, Supporting Information) reveals that different Zn sites in ZIOS have inhomogeneous bond valence, suggesting that these sites may show distinct transmetalation behaviors. Such a hypothesis aligns with our DFT calculations on thermodynamic favorability of transmetalation that we discuss as follows.

2.2. Mechanistic Insights: Distinct Cu²⁺/Ni²⁺ Preferential Adsorption Behaviors of ZIOS Membranes Probed with in situ Raman Spectroscopy

Our experimental adsorption results reveal that ZIOS membranes feature outstanding discrimination among transition metal ions. However, these experimental insights stem from an ex situ approach, wherein the quantification of the remaining cations in the supernatant occurs after the adsorption process. This approach, despite providing meaningful information, may not capture a complete spectrum of chemical or structural evolutions that ZIOS undergoes throughout the entire adsorption process. This stimulates us to employ in operando Raman spectroscopy to examine ZIOS membrane while it adsorbs a target ion of interest from different ion mixtures. with a setup shown in Figure S11. These results help unveil the realtime reaction mechanisms that exsitu characterizations cannot fully capture. Figure 3a shows the crystallographic structure of ZIOS that is formed through the coordinative binding of Zn²⁺ and organic ligands, i.e., Sal and MeIM. Given this structure, in addition to certain Raman-active vibrational bands originating from the ligands, we can anticipate the emergence of new Raman peaks, which would be indicative of the coordinative bonds between zinc and the ligands. To identify the characteristic vibrations of ZIOS, we initially contrast the Raman spectra of ZIOS with those of the isolated Sal and MeIM within the 110–1370 cm⁻¹ region (Figure S12a, Supporting Information). In particular, while molecular vibrations linked to the organic ligands predominantly manifest from 650 to 1370 cm⁻¹, [16] the specific region spanning 110–610 cm⁻¹ (Figure S12b, Supporting Information) reveals the emergence of new peaks at 382 and 590 cm⁻¹, implying the zinc-oxygen Zn-O_{phenolate} and Zn-O_{hydroxyimino} bonding, respectively. This Zn(II)-O interaction is further confirmed by contrasting the Raman spectrum of ZIOS with that of Zn/Sal complex (Figure S12b, Supporting Information). Similarly, the Raman spectrum of ZIOS with that of Zn/MeIM indicates that the peak at 147 cm⁻¹ is associated with the characteristic band of Zn-N_{MeIM} interaction, supported by literature. [17] Notably, the peak positions of Zn-N_{MeIM}, $Zn-O_{phenolate}$, and $Zn-O_{hydroxyimino}$ align closely with our DFT-computed vibrational frequencies assigned for the corresponding bonds (Table S4 and S5, Supporting Information).

Importantly, there are several fundamental insights that one needs to conceive to employ Raman spectrum effectively to reveal the adsorption mechanisms: 1) Raman vibrational bands are associated with the presence of bonds or a specific compound; therefore, the appearance of new bands can provide insight into the exact cause of the structural reconfiguration; 2) peak shifts often indicate a change in the chemical composition due to chemical interactions, structural transition of materials, interfacial species on the surface; and 3) absolute Raman intensity, inevitably affected by substrates, sample quality, or laser polarization



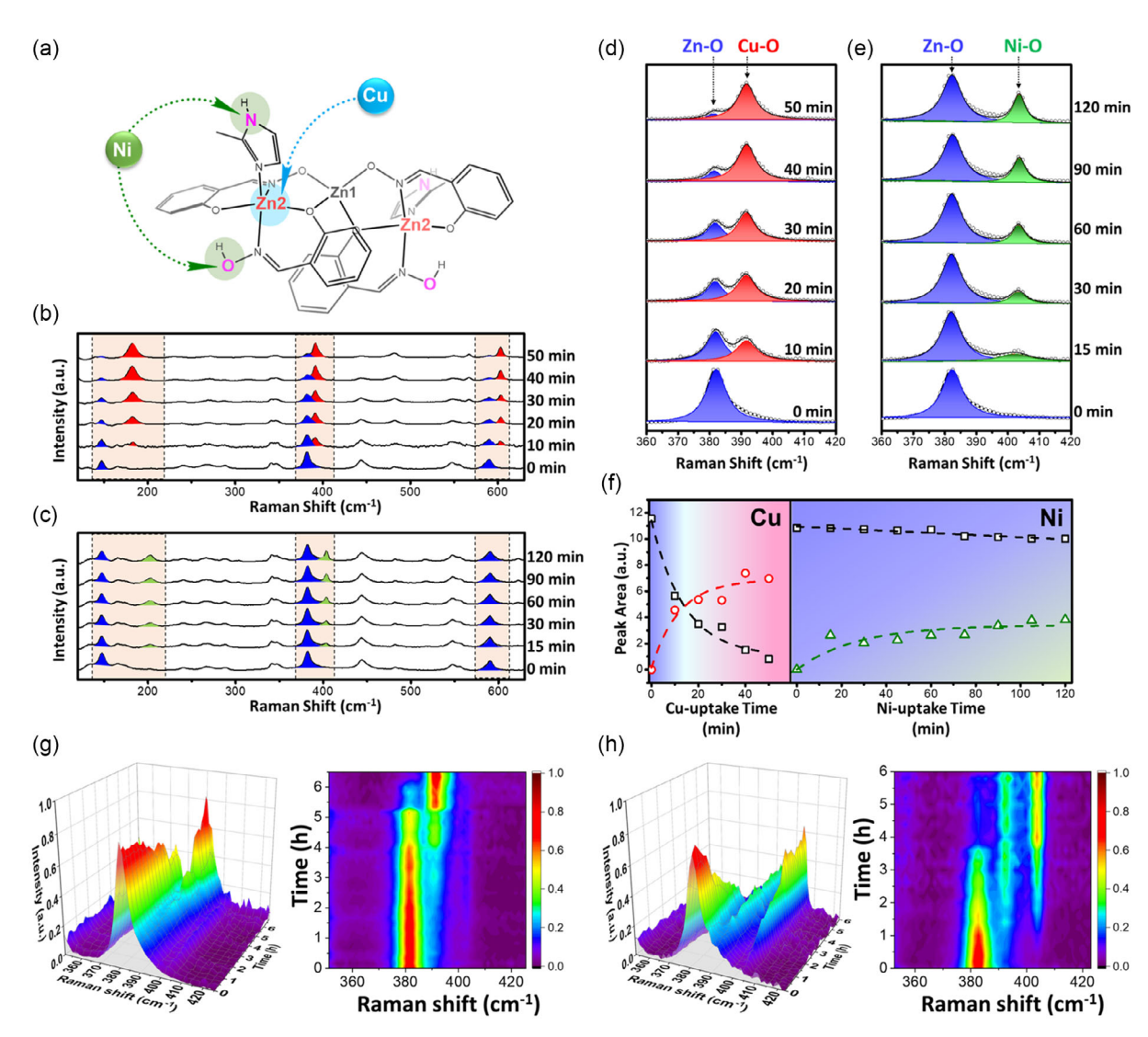


Figure 3. a) The proposed differentiation of adsorption mechanisms between Cu²⁺ and Ni²⁺. In situ Raman analysis of ZIOS/PVDF-PDA-PEI membrane when exposed to aqueous solution of single ions: b,d) Cu²⁺ ion at 400 ppm (pH 5.0) and c,e) Ni²⁺ ion at 400 ppm (pH 5.0). Note: f) Correlation between the peak area of Cu bonded (at 391 cm⁻¹, red open circle) and Ni bonded (at 404 cm⁻¹, green open triangle) versus zinc bonded (382 cm⁻¹, black open square) in ZIOS calculated from (d,3e). In situ Raman analysis of ZIOS/PVDF-PDA-PEI membrane when exposed to mixture ions with equimolar aqueous solution of Cu²⁺, Ni²⁺, Co²⁺, and Mn²⁺ (100 ppm each) at pH g) 2.5 and h) 5.0. Sample size is 5 × 5 mm², and the experiment was duplicated.

may lead to certain discrepancies. In this regard, the relative intensity ratio is considered a more objective factor to evaluate the adsorption mechanism. As part of the control experiments, the membranes were immerged in solutions of varying pH levels (2.5 and 5.0) prior to in situ Raman tests. The results indicate that the Raman spectrum of ZIOS/PVDF-PDA-PEI membranes remains largely unchanged even after a duration of 5 h, pointing to no observable pH-induced alterations (Figure S12c,d, Supporting Information). Since the adsorption of multiple ions is rather complicated to investigate, we first inspect in situ Raman responses on single-cation adsorption of ZIOS membranes before further exploring the complexities of their multiple-ion adsorption behaviors. Accordingly, a series of in situ Raman spectra are collected during the adsorption experiments of ZIOS toward Cu, Ni, Co, and Mn ions (Figure 3b-e and

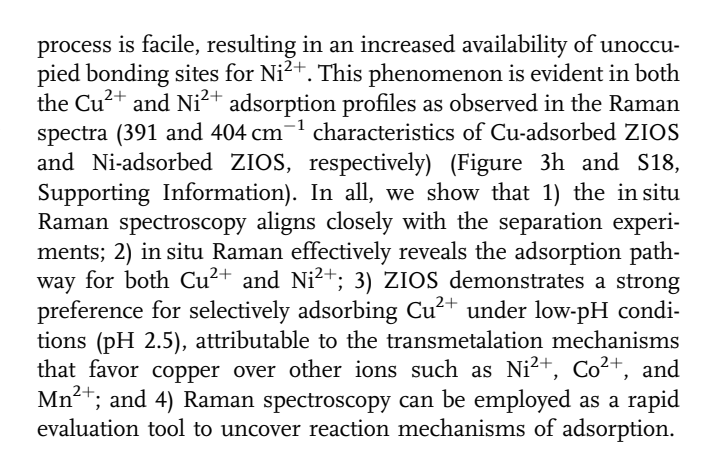
S14-16, Supporting Information). Figure 3b shows the in situ Raman of ZIOS throughout the Cu(II) ion adsorption process. The distinct Raman vibrations of ZIOS originating from $Zn-N_{MeIM}$, $Zn-O_{phenolate}$, and $Zn-O_{hydroxyimino}$ at 147, 382, and 590 cm⁻¹, respectively, are clearly visible at the beginning. Intriguingly, following a 10 min adsorption period, the concurrent emergence of three new peaks at 182, 391, and 603 cm⁻¹ is observed. As these peaks undergo progressive evolution throughout the course of adsorption, the Zn-to-ligand vibrational bands of ZIOS gradually diminish. The decrease in intensity of $Zn-N_{MeIM}$, $Zn-O_{phenolate}$, and $Zn-O_{hydroxyimino}$ at 147, 382, and 590 cm⁻¹, coupled with the emergence of the new peak set, suggests that Zn within Zn- N_{MeIM} , Zn- $O_{phenolate}$, and Zn-O_{hydroxyimino} bindings were continually replaced with external stimuli such as protons from the acidic media or with Cu(II)



www.advancedsciencenews.com

ions. Note that the difference between these vibrations is in the range of 9–35 cm⁻¹, suggesting that these differences are caused by the changes in the chemical composition of the bonding. Namely, Zn(II) ions within the framework of ZIOS are gradually transmetalated with Cu(II) ions from the solution. Figure 3c depicts the in situ Raman analysis of Ni(II) ions adsorption on ZIOS, revealing the emergence of two new peaks at 202 and 404 cm⁻¹ which appear to be characteristics of Ni–N and Ni–O, respectively (confirmed with DFT-computed vibration frequencies in Table S4 and S5, Supporting Information). Figure 3d,e shows the disparities within the Cu(II) and Ni(II) adsorption mechanisms on ZIOS, and these distinctions can be further elucidated through an in-depth analysis of the peak at 382, 391, and 404 cm⁻¹. Figure 3f demonstrates a significant difference in the correlation between the peak area estimated from the Raman identity spanning 360-420 cm⁻¹ (Figure 3d,e) of Zn-O_{phenolate} (382 cm⁻¹, characteristic of ZIOS), Cu-O (391 cm⁻¹), and Ni-O (404 cm⁻¹) in single-ion adsorption in operando Raman tests. Namely, the characteristic peaks of ZIOS are preserved, accompanied by the gradual evolution of Ni—N and Ni—O peaks in the case of Ni(II) ion adsorption. We speculate that the emerging Ni-O peak at 404 cm⁻¹ is more likely characteristic of Ni-O_{hydroxyimino} because these sites remain open and active to coordinate with the guest Ni²⁺ ion while the O_{phenolate} sites remain intact in their bonding with zinc, evidenced by the unchanged Raman intensity of Zn-O_{phenolate} peaks in ZIOS with time (Figure 3e). In contrast, for the Cu(II) ions adsorption scenario, the Zn-O_{phenolate} peaks of ZIOS exhibit a significant decrease, accompanied by a pronounced increase in the Cu-O peak intensity. This Cu-O peak at 391 cm⁻¹ is, thus, more likely characteristic of Cu-O_{phenolate}. Also, the adsorption of Cu happens more rapidly than Ni²⁺ does. The in situ Raman data thus highlight the distinct adsorption behaviors observed between the two metal ions Ni(II) and Cu(II) (Figure 3a). This distinct adsorption behavior suggests that Ni^{2+} negligibly replaces zinc within ZIOS frameworks but, instead, binds to unoccupied binding sites (O and N), originating from Sal or MeIM, respectively. In contrast, the in situ Raman spectra during Co2+ and Mn2+ adsorption reveal no discernible differences (Figure S16, Supporting Information). We hypothesize that Co²⁺ and Mn²⁺ are weakly bound to the ZIOS structure through either transmetalation or ligand coordination mechanisms. Further deconvolution of Raman peaks may enable the quantification of Cu²⁺ or Ni²⁺ adsorption capacity and kinetics. Raman spectroscopy is thus proposed to be a rapid and effective tool for probing and analyzing time-resolved adsorption process.

Next, we conducted in situ Raman analyses for adsorption behaviors of ZIOS membranes in multi-ionic (Cu²⁺, Ni²⁺, Co²⁺, and Mn²⁺) solutions at pH 2.5 and 5.0. At pH 2.5, selective copper adsorption is observed for ZIOS through transmetalation, as seen in the considerable decrease of Raman intensity of Zn binding (382 cm⁻¹, characteristic of ZIOS) and the evolution of Cu binding (391 cm⁻¹, characteristic of Cu-adsorbed ZIOS) (Figure 3g and S17, Supporting Information). These changes in Raman responses indicate a stronger metal–ligand bonding in the Cu-transmetalated ZIOS, firmly evidenced by an equivalent blueshift of the DFT-calculated vibrational frequencies of corresponding bonds upon the copper adsorption (Table S4 and S5, Supporting Information). At pH 5.0, the deprotonation



2.3. The Gibbs Free Energy of Transmetalation and its Correlation with the Charge Difference

While experimental results confirmed the interplay between transmetalation and ligand coordination in the selective adsorption behaviors of ZIOS membranes to a given extent, in the following, we report DFT-based electronic structure calculations that provide mechanistic insights into how each of these mechanisms happen and compete. We first elucidate how the preferential binding behaviors of ZIOS membranes are governed by transmetalation. To obtain atomic insights into transmetalation, we probe the metal-ion exchange at two different types of Zn sites in the ZIOS structure (i.e., M1 and M2 in Figure 4). Different from the metal at the M1 site that is coordinated with four oxygen, the metal occupying the M2 site has five chemical bonds (M-2O_{phenolate}, M-2N_{oxime}, and M-N_{MeIM}). We find that the thermodynamics of transmetalation is the most favored for Cu at both sites followed by that of Ni at the M2 site. Meanwhile, the introduction of Co and Mn is hindered at both sites. This trend in reaction energy aligns with the experimentally observed selectivity of metal ion adsorption at the low-pH condition and thus explains the distinct performance of ZIOS in capturing Cu²⁺ via transmetalation. Furthermore, the DFT-calculated vibration of the M—O_a bond stretching (Figure 4) shifts to a high frequency by 11 cm⁻¹ for Cu transmetalation at the M2 site (Table S5, Supporting Information), agreeing with the shift (9 cm⁻¹) observed in our in situ Raman analysis (Figure 3) for substitution of Zn-O_a by Cu-O_a. In contrast, the change of vibrational frequency is negligible when Zn at the M1 site is replaced by Cu. These results reveal that the M2 site should be mainly responsible for the Cu²⁺ incorporation at low-pH conditions (e.g., pH 2.5). As such, we focused on the M2 site for our following electronic structure analysis, unless otherwise mentioned.

To understand the physical reason of this thermodynamic trend of transmetalation, we analyzed the atomic charge of metal sites in both the original and M(II)-transmetalated ZIOS structures. As shown in Figure 4, the change of Gibbs free energy of transmetalation at the M2 site is linearly correlated with the difference in the Bader charge of the exchanged metal compared to that of the Zn. This trend is attributed to the electronic interaction between the given guest metal ion (after exchanged and structurally optimized) and the chelating atoms (Figure S20,



small structures

www.advancedsciencenews.com www.small-structures.com

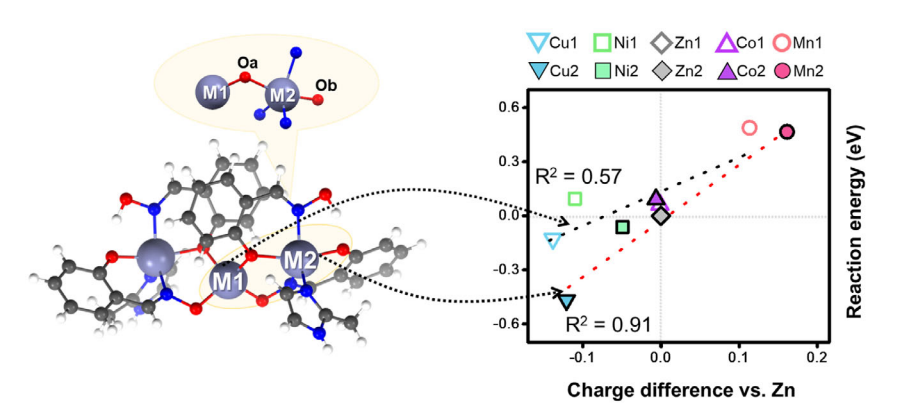


Figure 4. Gibbs free energy of transmetalation in the liquid phase and its correlation with the difference in Bader charge of metal ions, compared with Zn ion, at the M1 and M2 sites, both of which are labeled in the atomic structure. The metal, carbon, nitrogen, oxygen, and hydrogen are colored dark blue, grey, blue, red, and white, respectively.

Supporting Information). The metal ion (e.g., Cu) carries less positive charge in the transmetalated ZIOS and is more thermodynamically favorable to be exchanged into the framework, suggesting that the higher covalency of metal-ligand bonding should account for the enhanced stability of metal exchange.

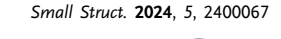
2.4. The Electronic Effect of Ligands on the Selectivity of Transmetalation

We further reveal the nature of metal-ligand bonds by decoupling the effect of three different chelating atoms on the electronic stability of metal coordination at the M2 site. Figure 5a shows the electron localization function (ELF) between a given guest metal at the M2 site and O_a and O_b atoms of the phenolate (denoted as M-2O bonds). Upon Cu transmetalation, the ELF at O_a and O_b atoms decreases. Meanwhile, the electron-rich domains (i.e., the ELF > 0.7) at these chelating atoms become more asymmetric and directional, rather than spherically distributed around the original Zn site. These changes in ELF indicate enhanced covalent characteristic of the corresponding Cu-ligand coordinations, [18] which aligns with the least positive charge accumulated at the Cu atomic site after being exchanged into the ZIOS framework. The covalency of M-2O bonds is less distinguished than that of the Zn-2O bonds upon the transmetalation of Ni, Co, and Mn. The trend is attributed to the overlap between the d-orbitals of different metals and the 2p-orbitals of O₂ and O_b. Figure S21, Supporting Information, shows that the d-orbitals of exchanged metals become more broadened and shift closer to the Fermi level ($E_{\rm f}$) than that of the original Zn site, increasing their overlap with the 2p orbitals of O_a and O_b chelators (Figure S22, Supporting Information). Furthermore, we observe that the Noxime and NMeIM chelators favor the covalency of their corresponding bonds with the Ni and Co ions, indicated by the better overlap between the d-orbitals of these metals and the 2p-orbitals of two corresponding chelators (Figure S23 and S24, Supporting Information). However, the increase appears less pronounced than that of M-2O_{phenolate} upon Cu transmetalation. These observations suggest that the oxygen of phenolate (i.e., O_a and O_b) should be responsible for the highest selectivity of Cu-ion exchanging.

Now we compare the bonding strength of the transmetalated M2-site by performing the projected crystal orbital Hamilton population (pCOHP) analysis in the M–2O_{phenolate}, M–2N_{oxime}, and M–N_{MeIM} bonds. For the M–2O_{phenolate} bond, Figure 5b shows that the -IpCOHP at E_f upon Cu transmetalation significantly increases, indicating stronger bonding, compared to that of the original Zn, while the latter is comparable with the Ni, Co, and Mn ion exchange. This difference is determined by the occupation of the antibonding state formed between the metal and oxygen chelators (Figure 5b). When a smaller M ion (i.e., Ni, Co, and Mn) is incorporated, yet the M–O distance remains the same for all these cases (Table S3, Supporting Information), the energy level of antibonding states is thus reduced relative to the $E_{\rm f}$ (Figure 5c). As a result, the occupation of these antibonding states is increased, destabilizing the M–2O_{phenolate} bonds.

It is noticed that the -IpCOHP at E_f of Ni—O and Mn—O bonding upon transmetalation is slightly higher than that of the Zn—O; however, this does not result from the less occupation of the antibonding states in corresponding interactions. Instead, such phenomena originate from the larger compensation of the –IpCOHP cumulative from the occupied bonding states of Ni–O and Mn—O interactions (the most positive values of the –IpCOHP profiles), which are all higher than that of the Zn—O. This is attributed to the more broadened *d*-orbitals of these exchanged metals, which increase their overlap with the *p*-orbitals of the O_{phenolate} ligand (Figure S21 and S22, Supporting Information).

We performed the same analysis of electronic structures for the M– $2N_{\rm oxime}$ and the M– $N_{\rm MeIM}$ interactions. The results showed that the corresponding bonding strength is also varied with the metal-ion exchanged (Figure S25 and S26, Supporting Information), yet less pronounced than that of M– $2O_{\rm phenolate}$ bonding upon the Cu transmetalation. However, it is worth noting that the metal ion upon transmetalation needs to stabilize their interactions with not only the $O_{\rm phenolate}$, but the other ligands (i.e., $N_{\rm Oxime}$ and $N_{\rm Mel}$). This explains the consistency between the bonding strength of overall metal–ligand interactions and the thermodynamic favorability of the metal-ion exchange (Figure 4 and S27, Supporting Information). In all, we showed that the enhanced strength of the metal– $O_{\rm phenolate}$



26884062, 2024, 8, Downloaded from https://onlinelibrary.wiley.com/doi/10.1002/sstr.202400067 by University Of Oklahoma, Wiley Online Library on [29/10/2024]. See the Terms and Condition

and-conditions) on Wiley Online Library for rules of use; OA articles are governed by the applicable Creative Commons License

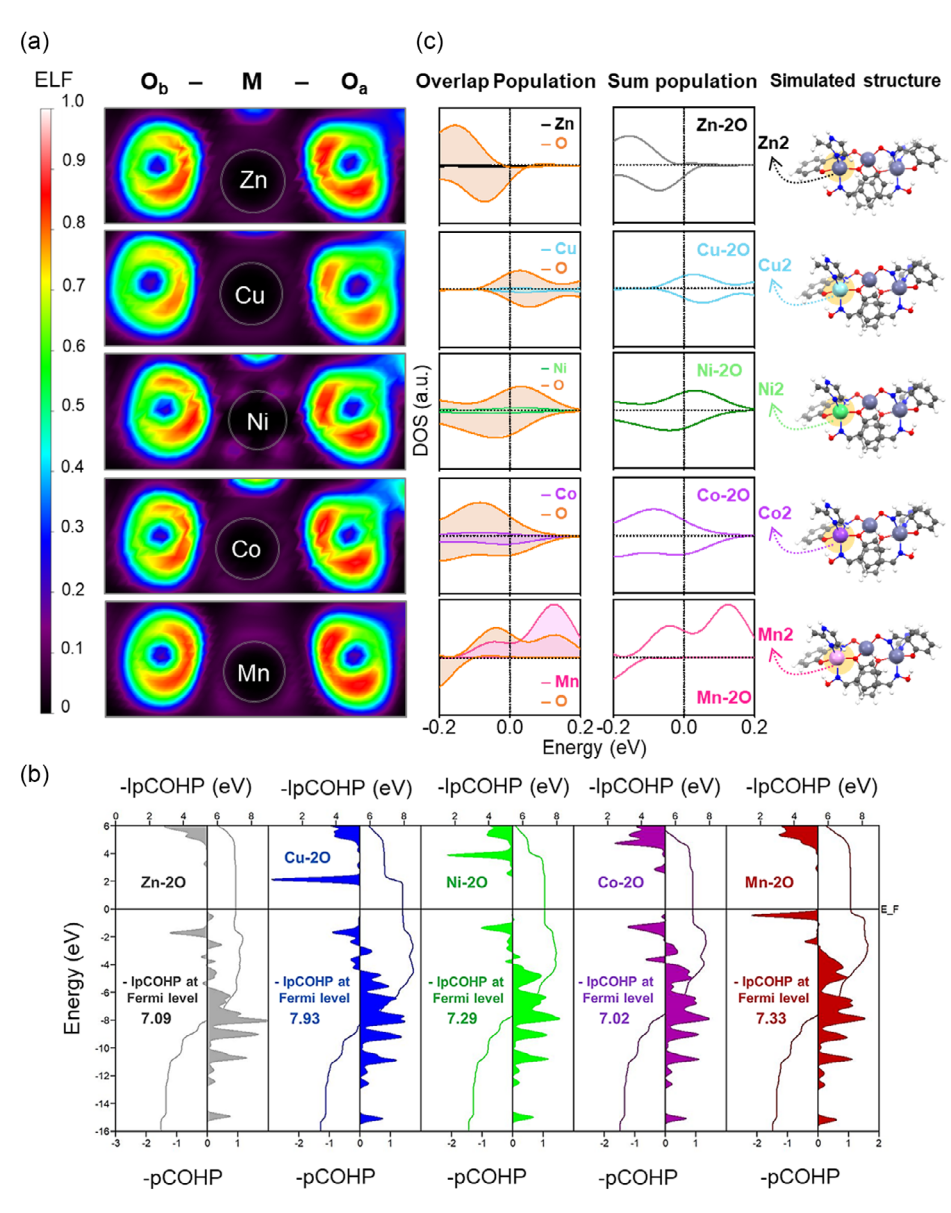


Figure 5. Electronic structure analysis of bonding between the metal and two oxygen chelators of phenolate ligands (M $-2O_{phenolate}$) at the M2 site. a) The ELF contour plot at the isosurface level of 0.70 e Å $^{-2}$; the brighter color corresponds to higher density of electrons. b) The COHP analysis including the projected COHP (pCOHP, the filled area) and its integration (IpCOHP, the curves). c) The projected density of states onto the metal and the $O_{phenolate}$ atomic sites to show the antibonding states of the M $-2O_{phenolate}$ bonds. The positive and negative density of state (DOS) represent spin up and down states, respectively.

bonding with minimal trade-off in that of the other metal-ligand interactions, which is determined by the hybridization of the metal d-orbitals with the chelator *p*-orbitals, is the key for increasing the selectivity of transmetalation in this study.

3. Conclusion

In this study, integrating in operando Raman spectroscopy with DFT calculations enables us to precisely identify binding sites and mechanisms that govern guest–host interactions within the local binding pockets of ions with similar properties. We have

identified thermodynamically favorable ion-exchange pathways and elucidated the selective order of transmetalation-based adsorption preferences in the ZIOS membrane with DFT simulations. Specifically, the distinct affinity of phenolate oxygen for Cu ions within the ZIOS framework plays a crucial role in the high selectivity of the membrane. In tandem, we demonstrate the synthetic controllability of membranes, where the physicochemical conditions of the synthesis medium are adjusted to convert 3D micrometer-scale crystals into a 2D crystalline selective layer on a composite membrane. Considering the slight ionic property differences between the competing ions (same charge and a size difference on the picometer scale),

www.advancedsciencenews.com



www.small-structures.com

achieving a $\text{Cu}^{2+}/\text{Ni}^{2+}$ separation factor of $\approx \! 200$ for our membrane is noteworthy. In all, the correlation of membrane binding preference with the electronic effects (e.g., orbital hybridization and electron localization) of ligands may shed light into the rational design of advanced functional materials for chemoselective separation, thereby shifting separation science toward a more precise regime.

Supporting Information

Supporting Information is available from the Wiley Online Library or from the author.

Acknowledgements

V.T.C.L. and Q.P.N. contributed equally to this work and share first authorship. This work was initiated and conducted with the support from OU startup budget. V.C.T.L. and N.T.B appreciate support by the Department of Energy, Energy Efficiency and Renewable Energy's Advanced Manufacturing Office, under National Alliance for Water Innovation (NAWI) hub (under Funding Opportunity Announcement DE-FOA-0001905, Award Number DE-AC02-05CH11231). B.W. appreciates support by the Department of Energy, Basic Energy Sciences (Grant DE-SC0018284). We thank Ms. Vy Nguyen for her assistance in refining a portion of the experimental writing section. Microscopy and powder X-ray diffraction (PXRD) data collection were performed at the Samuel Roberts Noble Microscopy Laboratory. In situ Raman characterization was performed at the School of Geosciences at the University of Oklahoma (OU). All density functional theory calculations were performed at the OU Supercomputing Center for Education & Research and the National Energy Research Scientific Computing Center (NERSC), a U.S. Department of Energy Office of Science User Facility.

Conflict of Interest

All authors declare no conflicts of interest. The membrane synthesis portion of this work was included in a pending patent submitted by NTB and VTCL.

Author Contributions

V.T.C.L. conducted the synthesis, characterization (scanning electron microscopy, energy dispersive X-ray spectroscopy, PXRD, (in situ) Raman, inductively coupled plasma-optical emission spectroscopy, adsorption tests, data analysis, presentation, and partial writing (experimental). Q.P.N. conducted the density functional theory (DFT) calculations: methodology, investigation, analysis, presentation, and partial writing (DFT). H.D.M. provided support on in situ Raman analysis and partial writing (in situ Raman). B.W. contributed in reviewing and editing. N.T.B. led the conceptualization, supervised the study, edited the manuscript, and provided insights into the work. All authors approved the final version of the manuscript.

Data Availability Statement

The data that support the findings of this study are available from the corresponding author upon reasonable request.

Keywords

adsorptive crystalline membranes, binding mechanisms, electron localization of ligands, in situ Raman, metal recoveries, precision ion separations

Received: February 10, 2024 Revised: April 20, 2024 Published online: May 15, 2024

- a) A. A. Uliana, N. T. Bui, J. Kamcev, M. K. Taylor, J. J. Urban,
 J. R. Long, Science 2021, 372, 296; b) R. M. DuChanois,
 N. J. Cooper, B. Lee, S. K. Patel, L. Mazurowski, T. E. Graedel,
 M. Elimelech. Nat. Water 2023, 1, 37.
- [2] K. Kim, D. Raymond, R. Candeago, X. Su, Nat. Commun. 2021, 12, 6554.
- [3] a) U.S. Geological Survey, Mineral Commodity Summaries 2022: U.S. Geological Survey, Reston, VA 2022, p. 202, https://doi.org/10.3133/mcs2022; b) D. Bauer, H. Khazdozian, J. Mehta, R. T. Nguyen, M. H. Severson, B. C. Vaagensmith, L. Toba, B. Zhang, T. Hossain, A. P. Sibal, 2023 Critical Materials Strategy, Idaho National Laboratory (INL), Idaho Falls, ID 2023.
- [4] a) R. Levin, C. M. Villanueva, D. Beene, A. L. Cradock, C. Donat-Vargas, J. Lewis, I. Martinez-Morata, D. Minovi, A. E. Nigra, E. D. Olson, L. A. Schaider, M. H. Ward, N. C. Deziel, J. Exposure Sci. Environ. Epidemiol. 2024, 34, 3; b) S. W. D. Turner, J. S. Rice, K. D. Nelson, C. R. Vernon, R. McManamay, K. Dickson, L. Marston, Nat. Commun. 2021, 12, 7254.
- [5] Z. Wang, L. Huang, X. Dong, T. Wu, Q. Qing, J. Chen, Y. Lu, C. Xu, Nat. Commun. 2023, 14, 261.
- [6] R. M. DuChanois, M. Heiranian, J. Yang, C. J. Porter, Q. Li, X. Zhang, R. Verduzco, M. Elimelech, Sci. Adv. 2022, 8, eabm9436.
- [7] a) H. Wu, Y. Wang, C. Tang, L. O. Jones, B. Song, X.-Y. Chen, L. Zhang, Y. Wu, C. L. Stern, G. C. Schatz, W. Liu, J. F. Stoddart, Nat. Commun. 2023, 14, 1284; b) J. G. O'Connell-Danes, B. T. Ngwenya, C. A. Morrison, J. B. Love, Nat. Commun. 2022, 13, 4497; c) J. J. M. Nelson, T. Cheisson, H. J. Rugh, M. R. Gau, P. J. Carroll, E. J. Schelter, Commun. Chem. 2020, 3, 7; d) J. Luo, X. Luo, M. Xie, H.-Z. Li, H. Duan, H.-G. Zhou, R.-J. Wei, G.-H. Ning, D. Li, Nat. Commun. 2022, 13, 7771; e) L. M. M. Kinsman, B. T. Ngwenya, C. A. Morrison, J. B. Love, Nat. Commun. 2021, 12, 6258; f) H. Wang, Y. Zhai, Y. Li, Y. Cao, B. Shi, R. Li, Z. Zhu, H. Jiang, Z. Guo, M. Wang, L. Chen, Y. Liu, K.-G. Zhou, F. Pan, Z. Jiang, Nat. Commun. 2022, 13, 7123; g) T. Liu, K. R. Johnson, S. Jansone-Popova, D.-E. Jiang, JACS Au 2022, 2, 1428; h) Y. Yuan, Y. Yang, K. R. Meihaus, S. Zhang, X. Ge, W. Zhang, R. Faller, J. R. Long, G. Zhu, Nat. Chem. 2023, 15, 1599.
- [8] T. Ye, G. Hou, W. Li, C. Wang, K. Yi, N. Liu, J. Liu, S. Huang, J. Gao, Nat. Commun. 2021, 12, 5231.
- [9] R. Epsztein, R. M. DuChanois, C. L. Ritt, A. Noy, M. Elimelech, Nat. Nanotechnol. 2020, 15, 426.
- [10] P. Srimuk, X. Su, J. Yoon, D. Aurbach, V. Presser, Nat. Rev. Mater. 2020, 5, 517.
- [11] a) M. Wang, X. He, E. Hoenig, G. Yan, G. Peng, F. Shi, J. Radhakrishnan, G. Hill, D. M. Tiede, H. Zhou, C. Liu, iScience 2022, 25, 104044. b) Z. Wang, A. Sim, J. J. Urban, B. Mi, Environ. Sci. Technol. 2018, 52, 9741.
- [12] N. T. Bui, H. Kang, S. J. Teat, G. M. Su, C.-W. Pao, Y.-S. Liu, E. W. Zaia, J. Guo, J.-L. Chen, K. R. Meihaus, C. Dun, T. M. Mattox, J. R. Long, P. Fiske, R. Kostecki, J. J. Urban, *Nat. Commun.* 2020, *11*, 3947.
- [13] R. M. DuChanois, C. J. Porter, C. Violet, R. Verduzco, M. Elimelech, Adv. Mater. 2021, 33, 2101312.



small structures

www.advancedsciencenews.com www.small-structures.com

- [14] P. Kumar, D. W. Kim, N. Rangnekar, H. Xu, E. O. Fetisov, S. Ghosh, H. Zhang, Q. Xiao, M. Shete, J. I. Siepmann, T. Dumitrica, B. McCool, M. Tsapatsis, K. A. Mkhoyan, *Nat. Mater.* 2020, 19, 443.
- [15] a) J. R. Werber, C. Peterson, D. F. Stipanic, M. A. Hillmyer, Environ. Sci. Technol. 2022, 56, 17352. b) H. Duan, S. Wang, X. Yang, X. Yuan, Q. Zhang, Z. Huang, H. Guo, Chem. Eng. Res. Des. 2017, 117, 460. c) H. Duan, H. Liu, C. Hu, X. Yang, X. Wang, RSC Adv. 2020, 10, 18860. d) S.-Y. Tang, Y.-R. Qiu, Chemosphere 2019, 236, 124330; e) A. Yousaf, A. M. Arif, N. Xu, J. Zhou, C.-Y. Sun, X.-L. Wang, Z.-M. Su, J. Mater. Chem. C 2019, 7, 8861; f) S. Bensaadi, N. Nasrallah, A. Amrane,
- M. Trari, H. Kerdjoudj, O. Arous, M. Amara, *J. Environ. Chem. Eng.* **2017**, 5, 1037; g) M. Mokhtar, S. E. Dickson, Y. Kim, W. Mekky, *J. Ind. Eng. Chem.* **2018**, *60*, 475.
- [16] M. A. Elbagerma, H. G. M. Edwards, G. Azimi, I. J. Scowen, J. Raman Spectrosc. 2011, 42, 505.
- [17] Z. Öztürk, M. Filez, B. M. Weckhuysen, Chem. Eur. J. 2017, 23, 10915.
- [18] A. Savin, R. Nesper, S. Wengert, T. F. Fässler, Angew. Chem., Int. Ed. Engl. 1997, 36, 1808.
- [19] Y. Marcus, J. Chem. Soc., Faraday Trans. 1991, 87, 2995.



Small Struct. 2024, 5, 2400067